OXFORD

GENERAL ARTICLE

Regulation of phagolysosomal activity by miR-204 critically influences structure and function of retinal pigment epithelium/retina

Congxiao Zhang[1,‡], Kiyoharu J. Miyagishima[1,‡], Lijin Dong[2], Aaron Rising[3], Malika Nimmagadda[3], Genqing Liang[3], Ruchi Sharma[3], Roba Dejene[3], Yuan Wang[1,#], Mones Abu-Asab[4], Haohua Qian[5], Yichao Li[5], Megan Kopera[2], Arvydas Maminishkis[1], Jennifer Martinez[6] and Sheldon Miller[1,*]

[1]Ophthalmic Genetics and Visual Function Branch, Section on Epithelial and Retinal Physiology and Disease, National Eye Institute, National Institutes of Health, Bethesda, MD 20892, USA, [2]Genetic Engineering Facility, National Eye Institute, National Institutes of Health, Bethesda, MD 20892, USA, [3]Ophthalmic Genetics and Visual Function Branch, Unit on Ocular and Stem Cell Translational Research, National Eye Institute, National Institutes of Health, Bethesda, MD 20892, USA, [4]Section of Histopathology, National Eye Institute, National Institutes of Health, Bethesda, MD 20892, USA, [5]Visual Function Core, National Eye Institute, National Institutes of Health, Bethesda, MD 20892, USA and [6]Inflammation and Autoimmunity, National Institute of Environmental Sciences, National Institutes of Health, Bethesda, MD 20892, USA

*To whom correspondence should be addressed at: National Eye Institute, National Institutes of Health, 31 Center Dr., MSC 2510, Bethesda, MD 20892, USA. Tel: (301) 4516763; Fax: (301) 4515421; Email: MillerS@nei.nih.gov

Abstract

MicroRNA-204 (miR-204) is expressed in pulmonary, renal, mammary and eye tissue, and its reduction can result in multiple diseases including cancer. We first generated miR-204$^{-/-}$ mice to study the impact of miR-204 loss on retinal and retinal pigment epithelium (RPE) structure and function. The RPE is fundamentally important for maintaining the health and integrity of the retinal photoreceptors. miR-204$^{-/-}$ eyes evidenced areas of hyper-autofluorescence and defective photoreceptor digestion, along with increased microglia migration to the RPE. Migratory Iba1^{+} microglial cells were localized to the RPE apical surface where they participated in the phagocytosis of photoreceptor outer segments (POSs) and contributed to a persistent build-up of rhodopsin. These structural, molecular and cellular outcomes were accompanied by decreased light-evoked electrical responses from the retina and RPE. In parallel experiments, we suppressed miR-204 expression in primary cultures of human RPE using anti-miR-204. *In vitro* suppression of miR-204 in human RPE similarly showed abnormal POS clearance and altered expression of autophagy-related proteins and Rab22a, a regulator of endosome maturation. Together, these *in vitro* and *in vivo* experiments suggest that the normally high levels of miR-204 in RPE can mitigate disease onset by preventing generation of oxidative stress and inflammation originating from intracellular accumulation of undigested photoreactive POS lipids. More generally, these results implicate RPE miR-204-mediated regulation of autophagy and endolysosomal interaction as a critical determinant of normal RPE/retina structure and function.

Introduction

It is now recognized that microRNAs (miR) control 30% of mammalian protein-coding genes (1) and are fundamentally important regulatory elements that can provide homeostatic control of cell function and its extracellular environment via autonomous and non-autonomous mechanisms. miRs such as miR-204 are highly conserved and target specific messenger RNAs (mRNAs) that support a variety of tissue-specific functions (2–9). Dysregulation of these regulatory elements is the basis of multiple disease processes throughout the body.

miR-204 resides in an intron of the TRPM3 (transient receptor potential cation channel) gene and has been shown to be frequently downregulated in a host of cancers including breast, colorectal, lung and acute myeloid leukemia consistent with a tumor suppressive role (4,5,10,11). In breast cancer, miR-204 downregulation has been associated with more aggressive tumors and poor prognosis (12) and its targets include genes involved in proteolysis, endopeptidase activity, cell adhesion, cell cycle phase and cell proliferation (13). In cancer, downregulation of miR-204 fuels tumor growth by initiating autophagic activity and increasing nutrients recycled from degraded intracellular structures (6). Similarly, in an *in vitro* model of gastric cancer, evidence suggests that miR-204 is protective against transforming growth factor β (TGF-β)-induced epithelial–mesenchymal transition (EMT) (14). In diabetic models, miR-204 is frequently overexpressed resulting in inadequate insulin secretion (15). Furthermore, miR-204 has been shown to play an essential role in ocular development where an inherited mutation in its seed sequence leads to coloboma (2).

miR-204 is regulated independently of its host gene, TRPM3 (transient receptor potential cation channel subfamily M member 3), by epigenetic mechanisms that affect their coordinated expression (co-transcribed or separate) and perturbations in either can also manifest in non-cancer-related pathologies. For example, downregulation of miR-204 in lung results in pulmonary arterial hypertension, independent of TRMP3, and elicits cell proliferation and reduced apoptosis involving a STAT3 (signal transducer and activator of transcription 3)-dependent mechanism (3). In pancreatic islet β-cells, miR-204 is involved in downregulating MAF bZIP transcription factor A—a transcription factor for insulin production (15). However, similar to pulmonary arterial hypertension, TRPM3 does not participate in miR-204-mediated inhibition of insulin transcription (15).

The retinal pigment epithelium (RPE) is a monolayer of cells that comprise the outer blood retinal barrier, where it carries out diurnal phagocytosis of shed photoreceptor outer segments (POSs). It also plays a critical role in the visual cycle by maintaining the light sensitivity of photoreceptors through the regeneration and supply of 11-*cis*-retinal that restores the dark-adapted state of the visual pigment. This epithelium also helps to maintain the health of the photoreceptors and the choroid by regulating the volume and the chemical composition of the subretinal space (SRS). Previously, we showed that miR-204 is highly expressed in native adult and fetal human RPE and that transfection with anti-miR-204 increased apical membrane TGF-β receptor 2, a direct target of miR-204, and decreased Kir 7.1, an apical membrane K channel (9). These experiments showed that normally high miR-204 levels in human RPE function to maintain epithelial phenotype, including epithelial barrier function and cell polarity.

The present experiments show that miR-204$^{-/-}$ mice gradually develop significant structural and functional abnormalities associated with the pathological accumulation of rhodopsin in the RPE. These outcomes coincide with an increasing population of Iba1$^+$ microglial cells (16) migrating to the RPE, decreased outer segment digestion concomitant with autophagosome accumulation and the reduction in retinal/RPE light-evoked electrical responses. In primary cultures of human RPE, alterations in the phagocytic and endolysosomal pathways were further examined using anti-miR-204. In human RPE, miR-204 reduction decreased clearance of rhodopsin containing POSs. These findings are reminiscent of the changes observed in miR-204$^{-/-}$ mice and in patients with age-related macular degeneration (AMD) (17).

Results

RPE miR-204 is critical for preventing cellular responses such as EMT, cell migration and proliferation that can lead to a host of retinal dystrophies. Thus, we generated a loss-of-function mutation in mice by replacing the pre-miR-204 stem-loop sequence with a neomycin resistance cassette (Supplementary Material, Fig. S1a) through homologous recombination in mouse embryonic stem cells. The deletion allele, designated as knockout (KO), was confirmed by Southern blotting (Supplementary Material, Fig. S1b) and long genomic polymerase chain reaction (PCR) (Supplementary Material, Fig. S1c). miR-204$^{-/-}$ mice were identified by standard PCR conditions for genotyping deoxyribonucleic acid (DNA) extracted from tail biopsy (Supplementary Material, Fig. S1d). In germline-transmitted mice (miR-204$^{-/-}$), complete lack of miR-204 expression was demonstrated in the eye and brain by northern blotting (Supplementary Material, Fig. S1e). qRT-PCR measurements confirmed the lack of the mature form of miR-204 in the RPE and retina (Supplementary Material, Fig. S1f) of miR-204$^{-/-}$ mice (levels of miR-211 remain unchanged). mRNA levels of TRPM3 are unaffected by intragenic deletion of miR-204 (Supplementary Material, Fig. S1g). Deletion of pre-miR-204 did not lead to splicing alterations in the TRPM3 gene, determined by qRT-PCR using primers to exons that flank pre-miR-204 (Supplementary Material, Fig. S1h).

Retina and RPE structural changes in miR-204$^{-/-}$

miR-204$^{-/-}$ mice appear developmentally normal, and miR-204$^{-/-}$ males and females are fertile and able to produce normal sized litters without any significant effect on weaning age (~21 days) (data not shown). We further compared wild type (WT) and miR-204$^{-/-}$ mice to determine if there were any apparent structural changes in the RPE. These miR-204$^{-/-}$ mice appear to have normal gross anatomical structure at birth (data not shown) and are not notably different from WT upon fundoscopic examination at 6 weeks of age (Fig. 1a, upper). However, fundoscopic examination of miR-204$^{-/-}$ mice at 6 months of age revealed significant numbers of ocular spots relative to WT (Fig. 1a, lower). Similarly, fundus autofluorescent (FAF) images of 6-month-old miR-204$^{-/-}$ mice possessed AF deposits (white) distributed globally beneath the retinal vasculature, at the level of the RPE (Fig. 1b), in a pattern similar to the hypopigmented spots in the fundus observations. Supplementary Material, Figure S6a and b summarizes preliminary data in 9-month-old heterozygous littermates (miR-204$^{+/-}$). We observed fewer AF white spots (25%, $n=4$) than the miR-204$^{-/-}$ or even the complete absence of spots (75%, $n=4$). At this age, there is little phenotypic change between the heterozygous and WT littermates, suggesting that the
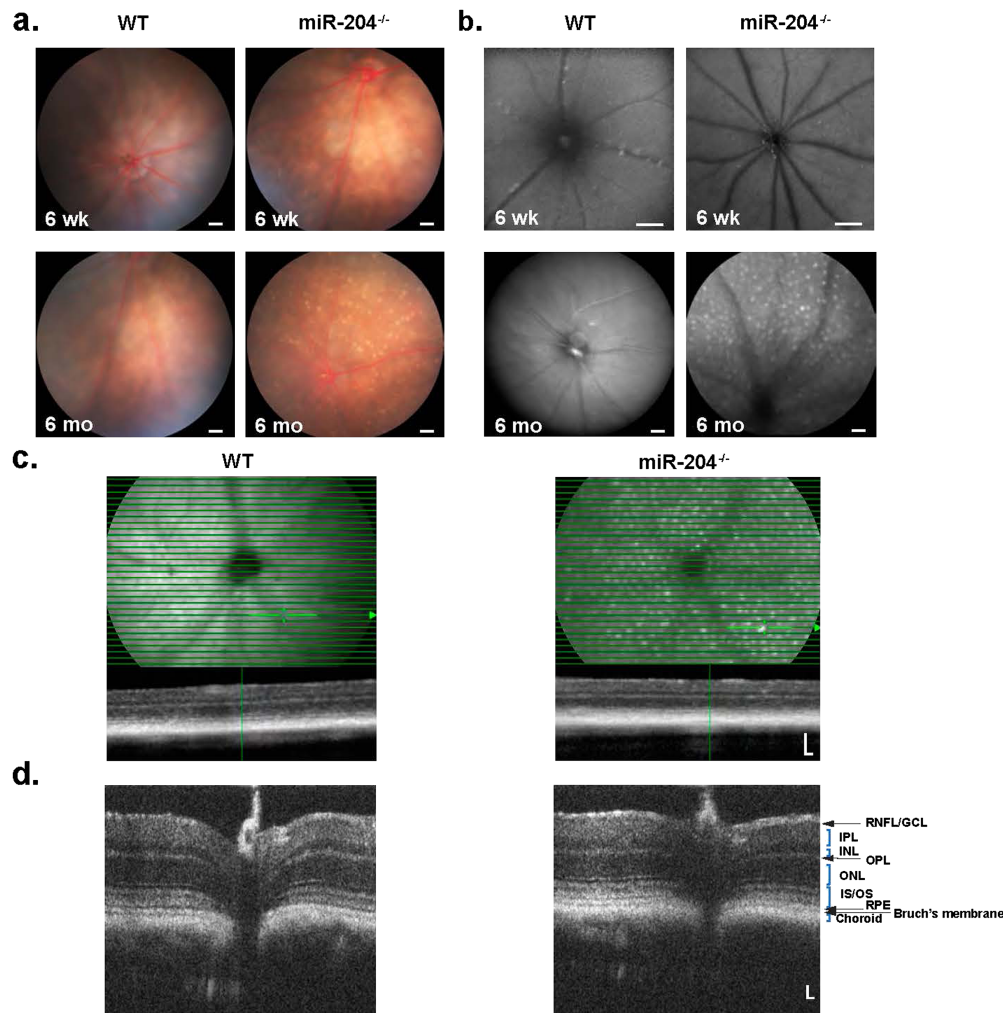
Figure 1. Fundus, AF and OCT images of WT and miR-204$^{-/-}$ mice. (**a**) Fundus images of 6-week-old mice show no abnormalities in WT (a, left) or miR-204$^{-/-}$ mice (a, right). However, 6-month-old miR-204$^{-/-}$ mice (a, lower right) show ocular spots, indicating damage to the RPE compared to WT (a, lower left). Scale bar, 200 μm. (**b**) FAF images at 6 weeks (b, upper) and 6 months (b, lower) show progressively increased AF deposits in the mir-204$^{-/-}$ compared to WT. Scale bar, 200 μm. (**c**) OCT images of 9-month-old WT (left panel) and miR-204$^{-/-}$ mice (right panel) show normal profiles and no obvious change in retinal structure. Scale bar, 100 μm. Thin horizontal lines indicate OCT scans, and image below is a transverse retinal section (Scale bar, 100 μm) at the location indicated by the cursor. The corresponding retinal anatomical structures are labeled. (**d**) HR OCT retinal images of WT and miR-204$^{-/-}$ reveal anatomical similarities in the thickness of the intraretinal layers identifiable by their hyperreflective bands.

normally high levels of miR-204 in the RPE are able to tolerate a 50% reduction in expression resulting in a milder phenotype compared to the KO (Supplementary Material, Fig. S6a, top).

Optical coherence tomography (OCT) images in WT, miR-204$^{+/-}$ mice and miR-204$^{-/-}$ mice (9-month-old), obtained using a Spectralis multi-modality diagnostic imaging system (Heidelberg Engineering, Fig. 1c; Supplementary Material, Fig. S6a, bottom), showed no obvious disruption in retinal structure. Additional images taken with sub-2 μm axial resolution (Envisu, Fig. 1d; Supplementary Material, Figure S6b) provided sufficient resolution to distinguish the retinal layers by reflectivity and optical intensity.

Microscopic study revealed age-related histopathological changes in the miR-204$^{-/-}$ relative to WT (Fig. 2a). Histological sections are compared between WT (left) and miR-204$^{-/-}$ (right) in 6-week-old (6 wk) and 10-month-old (10 mo), respectively. RPE cells of 6-week-old miR-204$^{-/-}$ mice appeared relatively normal (Fig. 2a, upper right panel), but by 10 months miR-

204$^{-/-}$ mice exhibited mis-localized cells in the SRS (Fig. 2a, black arrows, lower right panel) with additional disruption of the interphotoreceptor matrix (IPM).

We further examined ultrastructural changes that may be associated with the disruption of the IPM and the resulting accumulation of lipofuscin in 10-month-old miR-204$^{-/-}$ mice. Ultrastructural EM analysis of the RPE-photoreceptor boundary was performed for both the WT and miR-204$^{-/-}$ mice to identify additional RPE abnormalities in tissues collected at 12 p.m. (Fig. 2b, upper and lower images). Transmission electron microscopy (TEM) imaging in the WT displayed outer segments *en face* in the SRS adjacent to heavily pigmented melanosomes that populate nearby RPE cells. Figure 2b shows a lack of well-defined RPE basal infoldings (upper right panel, black arrow head), and the white arrow head shows a disrupted Bruch's membrane. Figure 2b (lower right panel) shows that at 10 months, there are more sparsely populated RPE melanosomes (white arrow) in the miR-204$^{-/-}$ mouse. Also, there is an overall disorganization of the IPM (black arrow).
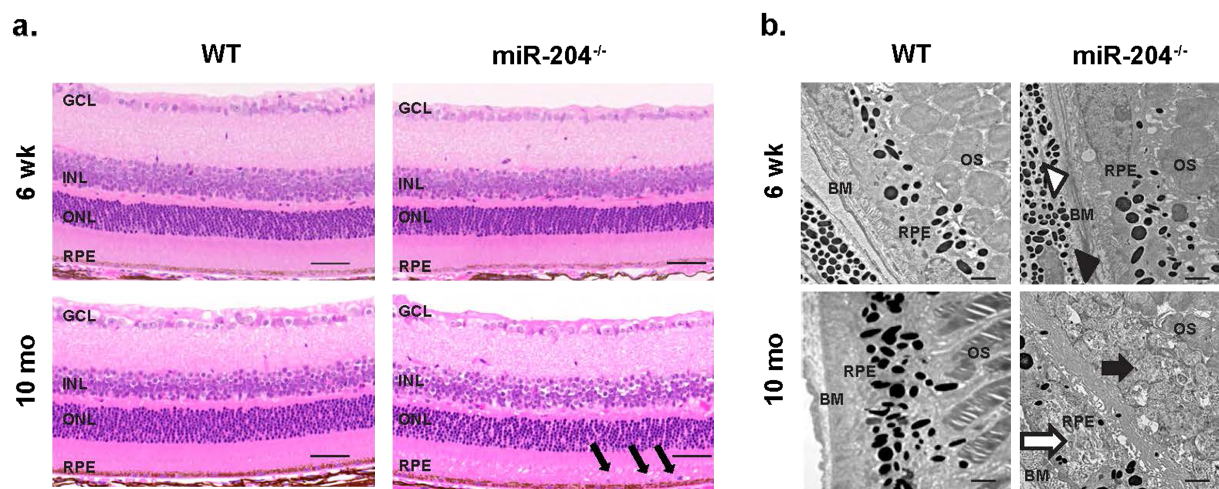
Figure 2. Abnormal subretinal deposits in miR-204$^{-/-}$ mice. (**a**) Light microscopic images of H&E stained 5 μm histological sections from WT (left) and miR-204$^{-/-}$ mice (right) at 6 weeks (top) and 10 months (bottom) displaying progressive changes in RPE cell junction integrity. The anatomic layers of the retina are labeled including the GCL, INL, and outer nuclear layers (ONL), in addition to the neighboring RPE. Black arrows mark abnormal cells in the SRS among misaligned outer segments. Scale bar, 50 μm. (**b**) Transmission electron micrograph images of the photoreceptor-RPE-choroid complex in the WT (left panel) and miR-204$^{-/-}$ mice (right panel). Upper left panel, image of WT RPE (6 weeks) with intact Bruch's membrane. Magnification, 10 000×. Scale bar, 1 μm. Lower left panel shows the individual melanosomes dispersed apically within the RPE (10 months). Note the distribution and shape (rounded and elliptical) of the melanosomes. Scale bar, 1 μm. Upper right panel depicting RPE from miR-204$^{-/-}$ mice (6 weeks) shows disrupted Bruch's membrane (open arrow head) and disorganization of the basal enfolding's (filled arrow head). Bottom right panel at 10 months shows disrupted photoreceptors in the SRS (filled arrow) and irregular melanosome distribution in the RPE (open arrow). Magnification, 10 000×. Scale bar, 1 μm.

Immunocytochemical staining of age-matched (6–8-month-old) cryosectioned mouse eyes using antibodies for photoreceptors (anti-rhodopsin and anti-opsin), microglial cells (anti-Iba1), bipolar cells (anti-PKCα) and ganglion cells (anti-BRN3A and anti-neural filament) revealed normal retinal organization in miR-204$^{-/-}$ mice phenotypically consistent with wild-type eyes (Supplementary Material, Fig. S2). Although miR-204 has been reported to be expressed in the ganglion and the inner nuclear layers (INLs) of the retina (18), the retinal thickness did not appear to be adversely affected in miR-204$^{-/-}$ mice (Supplementary Material, Fig. S2). In the WT, Iba1$^+$ microglia cells were selectively restricted to the inner plexiform layer (IPL), outer plexiform layer (OPL) and ganglion cell layer (GCL), while in the miR-204$^{-/-}$ eye the microglia population is larger and shows considerable regional variability (Supplementary Material, Fig. S2e) and increased presence at the SRS.

Retinal and RPE responses to light in miR-204$^{-/-}$

In addition to structural changes, miR-204$^{-/-}$ retina exhibited altered photoreceptor (a-wave) and bipolar cell (b-wave) response properties as measured by the electroretinogram (ERG). Light-evoked electrical responses from the RPE were obtained using direct couple (DC)-ERG recordings from the same mice whose retinal ERG a- and b-responses are summarized in Figure 3a–f. Averaged traces of dark-adapted ERG responses in age-matched (6–12-months-old) WT (black trace, $n = 24$ mice) and miR-204$^{-/-}$ mice (magenta trace, $n = 19$ mice) elicited by flashes of increasing intensity (0.0001–10 cd s/m^2) are shown in Figure 3a. The amplitudes of the dark-adapted ERG a- and b-waves were plotted as intensity-response curves (Fig. 3b and c). Mice lacking miR-204 displayed *decreased* a-wave responses at higher light intensities (0.1, 1 and 10 cd s/m^2) compared to the WT (*$P < 0.05$; Fig. 3b; Supplementary Material, Table S1), indicating alteration in photoreceptor activities. Similarly, Figure 3c shows that mice lacking miR-204 had a significant

reduction in their b-wave amplitudes (∼70% of age-matched WT controls) corresponding with reduced ON Bipolar cell activity (19) and smaller presynaptic rod responses (*$P < 0.05$; Fig. 3c; Supplementary Material, Table S2).

In Figure 3d, the averaged dark-adapted ERG responses elicited with 10 cd s/m^2 (Fig. 3a) are superimposed and scaled in amplitude to highlight changes in the kinetics of the light response on an expanded time scale. The time to peak is measured from the onset of the light stimulus to the minima (a-wave) or maxima (b-wave) of the ERG response. The dashed lines in Figure 3d illustrate the latency observed in the kinetics of the b-wave time to peak (10 cd s/m^2, *$P < 0.001$) in miR-204$^{-/-}$ mice ($\tau = 96.6 \pm 2.3$ ms) compared to WT ($\tau = 84.8 \pm 1.7$ ms). An analysis of the a-wave time to peak revealed no systematic differences between WT and miR-204$^{-/-}$ mice (Fig 3e) except at flash strengths of 1 cd s/m^2 (*$P < 0.05$). In contrast, the time to peak of the b-wave at the 3 highest light intensities (0.1, 1 and 10 cd s/m^2) was significantly delayed in miR-204$^{-/-}$ mice (*$P < 0.05$; Fig. 3f). By contrast, responses from heterozygous mice although decreased in amplitude and delayed in their time to peak compared to WT were less than that observed in the miR-204$^{-/-}$ as one would expect for a 50% reduction in miR-204 (Fig. S6c–h).

Using DC-ERG recordings generated by a transition from darkness to continuous light (7 min period of illumination at 10 cd/m^2), we obtained representative traces of the averaged RPE electrical responses (WT and miR-204$^{-/-}$ mice, Fig. 3g). This DC-ERG electrical response from the RPE contains four measurable components: c-wave, fast oscillation (FO), light peak (LP) and off response (OFF) as indicated in Fig. 3g. Supplementary Material, Figure S6i and j shows that there were no change in miR-204$^{+/-}$ mice compared to WT in the four components of the DC-ERG. In contrast, miR-204$^{-/-}$ mice showed detectable differences in the amplitudes of the c-wave and the FO. The data in Fig. 3g and h show that miR-204$^{-/-}$ mice (6–12-months-old; $n = 13$ mice; $n = 24$ eyes) undergo a significant decrease in RPE c-wave amplitude compared to age-matched
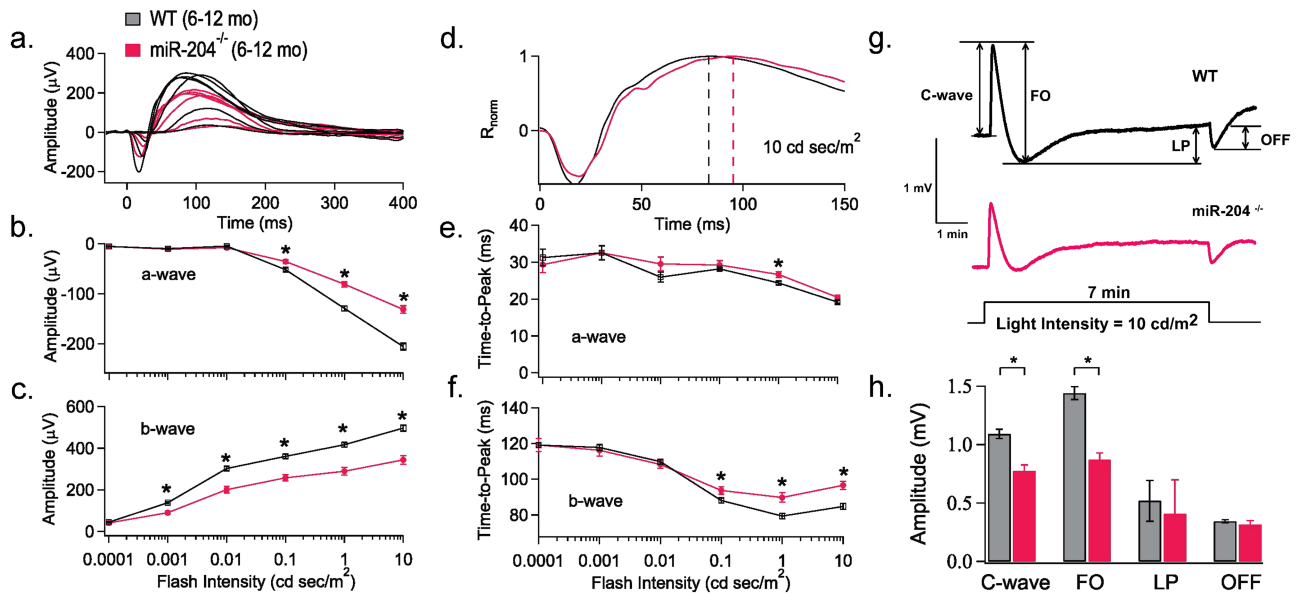
Figure 3. RPE and retina light responses in miR-204$^{-/-}$ mice. (**a**) Scotopic ERG responses elicited in response to stimuli of increasing flash intensities are averaged and superimposed to compare WT (black traces; 6–12 months; $n = 24$ mice) and miR-204$^{-/-}$ (magenta traces; 6–12 months; $n = 19$ mice) response properties. The corresponding dark-adapted a- and b-wave intensity-response curves for WT and miR-204$^{-/-}$ display reduced photoreceptor and bipolar cell activity (**b** and **c**). Significant decreases indicated by asterisks (*$P < 0.05$, Student's *t*-test). (**d**) The early portion of the ERG response elicited by a bright flash of 10 cd s/m^2 is replotted on an expanded time scale of 50 ms per division to highlight differences in response kinetics. Dashed lines indicate an 8 ms delay in the time to peak of the b-wave. (**e**) Time to peak of the a-wave plotted versus logarithm stimulus flash intensity in cd s/m^2. (**f**) Time to peak of the b-wave plotted versus logarithm stimulus flash intensity in cd s/m^2. Significant decreases indicated by asterisks (*$P < 0.05$, Student's *t*-test). (**g**) DC-ERGs of the RPE electrical response recorded from a WT ($n = 11$ mice, 6–12 months) and miR-204$^{-/-}$ mouse ($n = 5$ mice; 6–12 months), in response to a 7 min continuous light stimulus (10 cd/m^2), obtained by averaging all measurements from each group of mice. Arrows indicate c-wave, FO, LP and OFF. (**h**) Amplitudes of the DC-ERG components (c-wave, FO, LP and OFF) for WT (6–12 months, $n = 15$ mice, $n = 26$ eyes) and miR-204$^{-/-}$ (6–12 months, $n = 13$ mice; $n = 24$ eyes) mice recorded in response to a 7 min light stimulus (10 cd/m^2). Data reported as mean; error bars indicate standard error. *$P < 0.05$.

WT mice (6–12-months-old; $n = 15$ mice; $n = 26$ eyes) coincident with the first detectable changes in the ERG a-waves and b-waves (Fig. 3h; Supplementary Material, Table S3; *$P < 0.0001$). The *complete* absence of miR-204 also significantly reduced the FO component of the electrical response of the RPE (Fig. 3h; Supplementary Material, Table S3; $P < 0.0001$). Thus, miR-204 is necessary for the generation of two out of four of the light-induced electrical responses generated at the RPE apical and basolateral membranes (20).

Reduction in miR-204 is associated with accumulation of photoreceptor material and altered RPE endolysosomal function

In Figure 4a, the maximum intensity projection (MIP) (XZ—cross section) images of RPE from WT and miR-204$^{-/-}$ RPE collected at 8 a.m. indicated increased levels of RPE internalization of rhodopsin (red) that originated from phagocytosed POSs. Western blots probed with antibodies for rhodopsin indicate increased accumulation in the miR-204$^{-/-}$ RPE at 8 a.m. (2 h after light onset/peak of phagocytosis) and at 10 a.m. (Fig. 4b and c). Figure 4d shows resident microglial in the IPL and OPL of WT and miR-204$^{-/-}$ mice exhibiting long dendritic processes and small cell bodies. Iba1$^+$ microglial cells (in green) were imaged on the same plane as the apical surface of the RPE (Fig. 4e). In WT mice, there is a relative absence of microglia on the apical surface of the RPE. In contrast, numerous microglia, appearing amoeboid in shape, are shown resting on the apical surface of the RPE in miR-204$^{-/-}$ mice. Figure 4f is a three-dimensional reconstruction from image stacks of Iba1$^+$ microglial cells (in orange) with dendritic processes in physical contact with

the apical surface of the RPE stained with phalloidin (in green) in miR-204$^{-/-}$ mice (magnification, 100×). The arrow in Figure 4g shows that rhodopsin-labeled outer segments (in red) co-localized with Iba1$^+$-stained microglia with branched processes (in green) in miR-204$^{-/-}$ mice. Iba1$^+$ microglia cells likely originate from the INL and accumulate at the RPE apical membrane with altered morphology (Fig. 4e–g). This finding suggests that these migratory cells, normally not present in the SRS, can phagocytose POS and thus may contribute to the miR-204$^{-/-}$-induced autofluorescence signal shown in Figure 1b (21).

The considerable build-up of rhodopsin in RPE of miR-204$^{-/-}$ mice indicate either an increased rate of phagocytosis of shed outer segments or an impairment of phagolysosomal digestion, or both. To distinguish these possibilities and to explore the link between miR-204 levels and autophagy, we compared the expression levels of autophagy targets in RPE from three miR-204$^{-/-}$ mice ($n = 3$) and their WT littermates ($n = 4$). Surprisingly, ~34% (29/85) of the autophagy-related genes were overexpressed (greater than 2-fold compared to WT). Fourteen genes in addition to *Map 1lc3b* exhibited differential expression that was statistically significant ($P < 0.05$; Supplementary Material, Fig. S3a) most notably *Akt1*, *Atg3*, *Atg5*, *Atg9a*, *Eif4g1*, *Gabarapl2* and *Lamp1*. However, despite miR-204$^{-/-}$ mice displaying a significant increase in RPE mRNA expression of LC3/GABARAP family proteins (Supplementary Material, Table S4), western blots comparing protein levels of LC3B to WT indicate only a modest increase in LC3B-I and no observable difference in LC3B-II (Supplementary Material, Fig. S3b). These data are supported by the increased LC3B expression found in immunostained RPE in miR-204$^{-/-}$ mice at 8 a.m. and 10 a.m compared to WT (Supplementary Material, Fig. S5a and b). Taken together, these
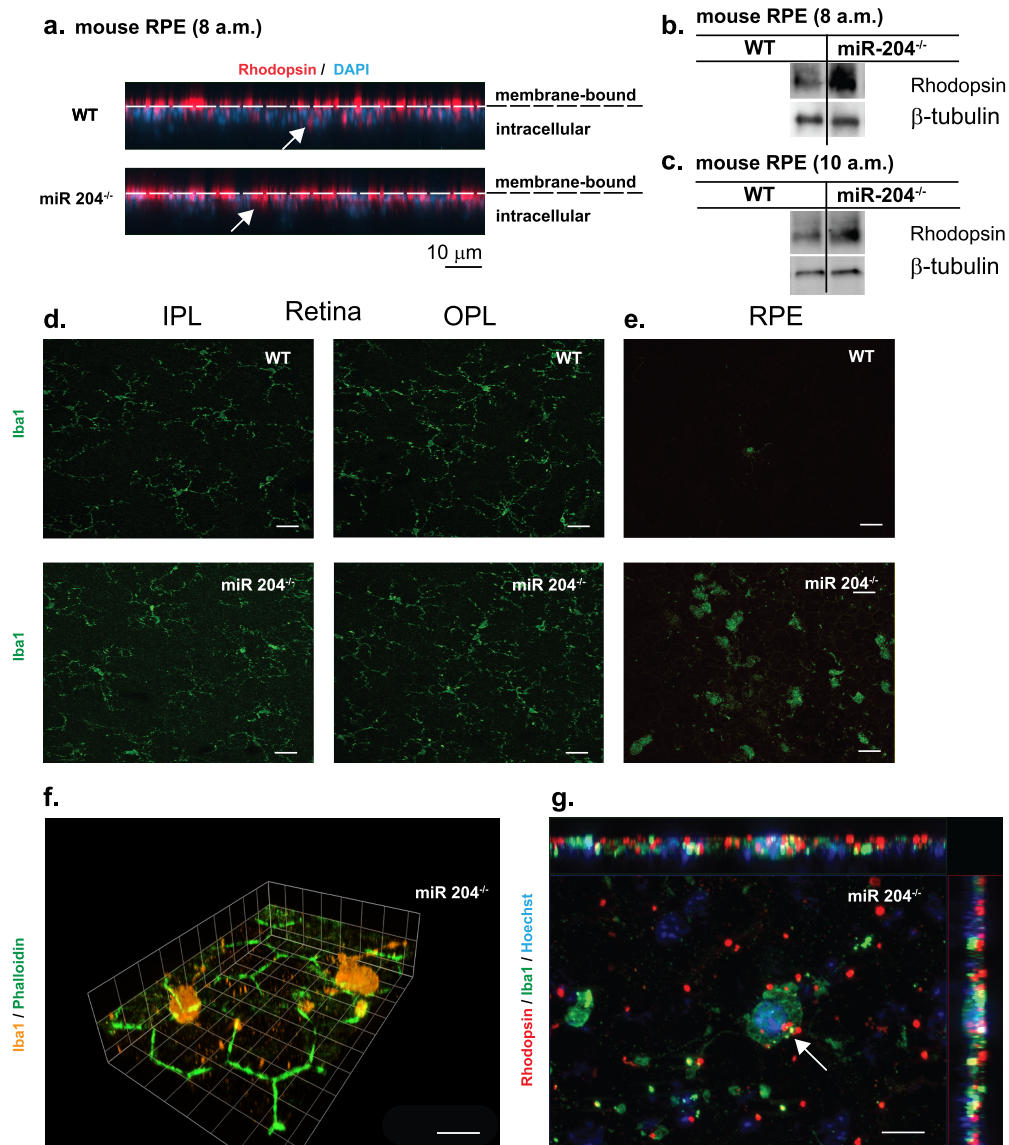
Figure 4. Increased rhodopsin accumulation and microglial activation in miR-204$^{-/-}$ mice. (**a**) Representative confocal images (XZ) of RPE whole mount tissues of 8- and 9-month-old WT and miR-204$^{-/-}$ mice (collected at 8 a.m.) immunostained for rhodopsin (red) and counterstained with DAPI. Dashed lines indicate boundary between membrane bound rhodopsin and internalized/intracellular rhodopsin. Scale bar, 10 μm. (**b** and **c**) Rhodopsin levels in the RPE of WT and miR-204$^{-/-}$ mice were measured by western blot ($n=5$ animals) at 8 a.m. or 10 a.m., respectively. (**d**) Resident microglia in the retina of wild-type and miR-204$^{-/-}$ mice. Iba1-labeled (green) microglial cells localized to IPL and OPL in WT and miR-204$^{-/-}$ mouse (8–9 months). Magnification, 40×. Scale bar, 20 μm. (**e**) Immunohistochemical staining for Iba1 (green) of RPE whole mount tissues from 8 to 9-month-old WT and miR-204$^{-/-}$ mice. Scale bar, 20 μm. (**f**) Iba1$^+$ (orange) microglial cells are shown infiltrating the apical surface of the RPE in the miR-204$^{-/-}$ mice. Phalloidin staining (green) reveals the RPE's regular hexagonal mosaic. Magnification, 100×. Scale bar, 10 μm. (**g**) Iba1$^+$ (green) microglial cells on the apical surface of the RPE in miR-204$^{-/-}$ mice co-localized (indicated by the white arrow) with rhodopsin (red). Nuclei labeled with Hoechst (blue). Magnification, 100×. Scale bar, 10 μm.

data indicate that although the expression of autophagy-related genes are elevated in miR-204$^{-/-}$ mice, they are not generally accompanied with a similar increase in LC3B-II.

To further examine the role of miR-204 in regulating phagolysosomal function and the clearance of phagocytosed outer segments, we used primary cultures of intact human RPE monolayers that closely approximate the physiology of native adult tissue (9,22–24). To reduce miR-204 expression we transfected these monolayers with anti-miR-204 for 4 or 9 days. Endogenous miR-204 knockdown was confirmed by RT-quantitative PCR (qPCR) to be >70% (9). At 4 days, post-transfection (Supplementary Material, Fig. S3c), western blots revealed increased levels of LC3B-I, but lacked an increase in LC3B-II, similar to miR-204$^{-/-}$ RPE. Interestingly, western blots probed for anti-GABARAPL2 (Supplementary Material, Fig. S4a and b), an LC3 analog, anti-Rubicon and anti-ATG14, markers for LC3-associated phagocytosis and canonical autophagy, respectively, did not reveal miR-204 dependent differences in expression (Supplementary Material, Fig. S4a). In contrast, in anti-miR-204 transfected RPE, the classic mTOR inhibitor, rapamycin, strongly promoted ULK1 phosphorylation, a key indicator of autophagy initiation compared to untreated and anti-miR-con controls (Supplementary Material, Fig. S3d). ULK1 regulates the lipidation status of LC3 by phosphorylating ATG4B and can contribute to the elevated LC3-I levels by converting convert LC3-II back to LC3-I (25,26).
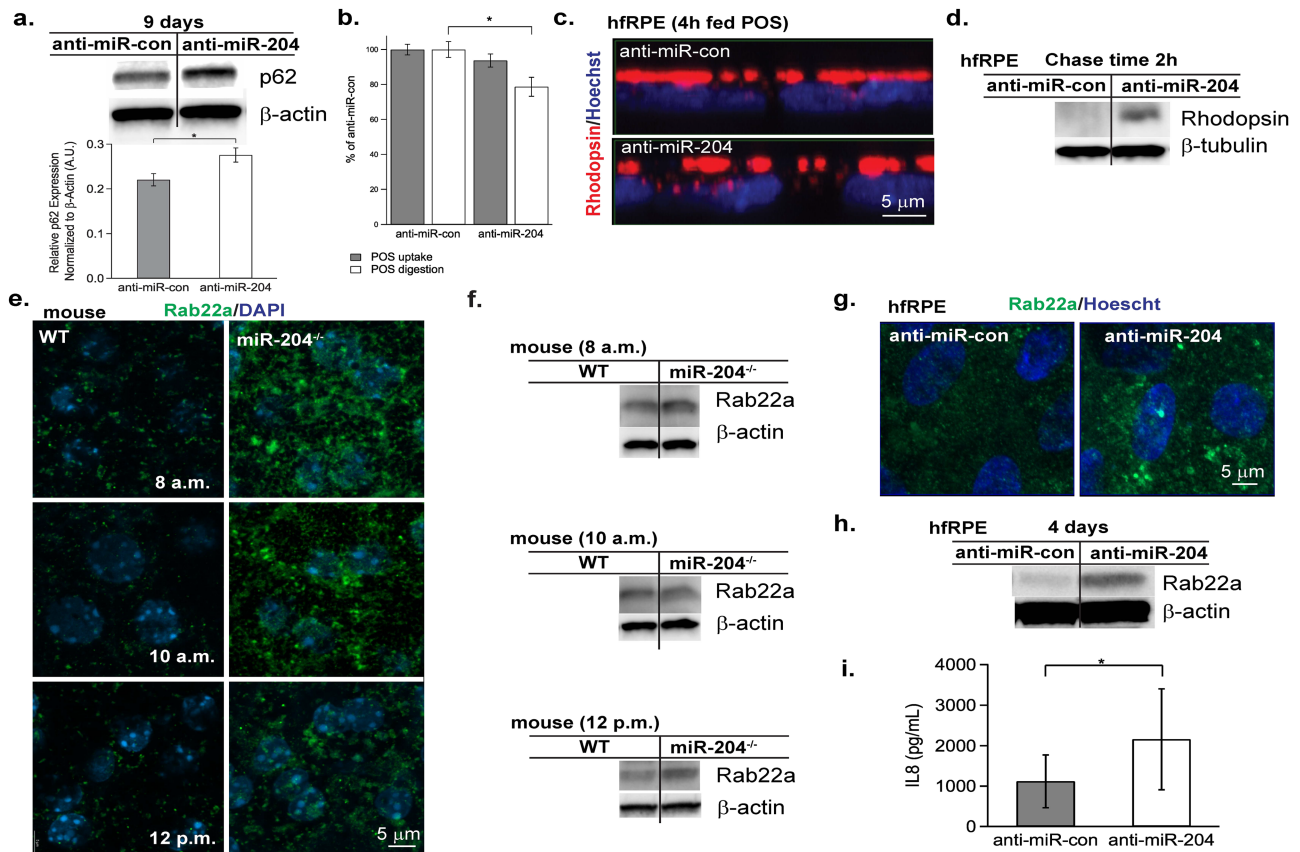
Figure 5. Autophagic and endolysosomal changes following reduction or complete loss of miR-204. hfRPE were transfected with anti-miR-204 or anti-miR-con for 4 or 9 days. At 9 days post-transfection (**a**, upper), Western blots of RPE protein lysate probed for p62 show elevation in anti-miR-204 samples compared to anti-miR-con (2 independent experiments). (a) p62 protein levels of RPE subjected to anti-miR-con ($n=4$) or anti-miR-204 ($n=4$) are normalized to β-Actin ($P=0.04$). (b) FACS quantification of internalized pHrodo-labeled bovine outer segments in hfRPE treated with anti-miR-204 or anti-miR-con for 4 days. POS uptake (gray bars) measured 4 h after feeding 10 POS/RPE. POS digestion (white bars) similarly measured following a 24 h chase. The digestion rate is significantly lower in the anti-miR-204 treated RPE with a P-value of 0.01. (c) Confocal images (XZ) of hfRPE 4 days post-transfection (anti-miR-con or anti-miR-204) following a 4 h feeding of 40 POS/RPE + MFG-E8 (2.5 μg/ml) + protein S (2 μg/ml) (63,64) prior to washing, fixation and staining for rhodopsin (red) and Hoechst 33342 (blue). (**d**) Western blot of hfRPE 4 days post-transfection (anti-miR-con or anti-miR-204) probed with rhodopsin after 4 h feeding of 40 POS/RPE + MFG-E8 (2.5 μg/ml) + protein S (2 μg/ml) followed by a 2 h chase period. (e) Immunofluorescence staining of Rab22a (green) and DAPI (blue) in RPE flat-mounts of WT and miR-204$^{-/-}$ mice obtained at 8 a.m., 10 a.m. and 12 p.m. Scale bar, 5 μm. (**f**) Representative Rab22a immunoblots of WT and miR-204$^{-/-}$ RPE, sampled at 8 a.m. ($n=4$), 10 a.m. ($n=4$) and 12 p.m. ($n=4$). (g) Immunofluorescence staining of Rab22a (green) and Hoechst 33342 (blue) in anti-miR-con and anti-miR-204 transfected hfRPE. Magnification, 63×. Scale bar, 5 μm. (**h**) Western blot of Rab22a expression in RPE from cell lysates taken from anti-miR-con and anti-miR-204-transfected hfRPE tissues (4 days post-transfection). (**i**) IL-8 levels, measured by Luminex bead-based multiplex assay, showed significant change in the apical media of hfRPE transfected with anti-miR-204 compared to anti-miR-con ($n=3$ donors, $P=0.02$, paired t-test).

At 9 days post-transfection (Fig. 5a), there were increased levels of p62—an autophagy adaptor protein and a marker for autophagosomes (27) in anti-miR-204 transfected RPE cells. p62 quantification was normalized to β-actin, and fold change was compared to anti-miR-con ($n=4$, $P=0.04$). p62 normally delivers ubiquitinated cargoes for autophagic degradation, and its elevation 9 days post-transfection suggests a block in the degradation pathway. In support of this notion, there is an increase in the number and size of undigested autophagosomes in TEM images of hfRPE transfected with anti-miR-204 (Supplementary Material, Fig. S3e) and mouse miR-204$^{-/-}$ RPE, collected at 8 a.m. and 10 a.m. compared to WT (Supplementary Material, Fig. S5c and d).

This *in vitro* approach of delivering anti-miR-204 also allowed us to determine whether miR-204 knockdown altered the rate of phagocytosis (at 4 days post-transfection), perhaps contributing to the accumulation of rhodopsin inside RPE cells. The results of pHrodo-labeled POS internalization or digestion in RPE cells are expressed as percentage of control (anti-miR-con). A Fluorescence-activated cell sorting (FACS) analysis of phagocytic consumption of pHrodo-labeled bovine outer segments following a single 4 h feeding (∼10 POS/RPE) revealed no detectable differences in phagocytic *uptake* between anti-miR-204 and the anti-miR-control (Fig. 5b, gray bars, $P>0.05$). A similar experiment was performed using pHrodo-labeled zymosan beads revealing that primary cultures of human fetal RPE do not participate in recognition and uptake of zymosan particles (Supplementary Material, Fig. S4c and d).

To assess rates of Rod outer segment (ROS) degradation, RPE were fed for 4 h followed by a 24 h chase period to ensure that all POS materials had been internalized and targeted for degradation. These data reveal that clearance of POS is reduced by ∼20% in the anti-miR-204 RPE cells compared to the anti-miR-con (Fig. 5b, white bars, $P=0.01$). This finding is supported by the increased number and size of autophagosome structures (28) in anti-miR-204 treated RPE (fed 40 POS/RPE) compared to anti-miR-con (Supplementary Material, Fig. S3e).

Additionally, similarly treated cells (fed either 10 or 40 POS/RPE) were fixed and stained for rhodopsin (Fig. 5c) and the lysosomal-associated membrane protein 2 (LAMP2, Supplementary Material, Fig. S3f), a lysosomal membrane marker. Immunofluorescence staining confirms rhodopsin accumulation inside anti-miR-204 RPE (Fig. 5c) and decreased number of lysosomes (shown in green) present in anti-miR-204 RPE following a 24 h period of digestion (Supplementary Material, Fig. S3f). A quantitative image analysis of LAMP2 signals is shown in Supplementary Material, Fig. S3g indicating a 1.6-fold higher expression in controls (anti-miR-con) compared to anti-miR-204 RPE ($P = 0.02$). Western blots of POS-fed RPE (40 POS/RPE) following a 2 h chase period confirm increased rhodopsin accumulation in the anti-miR-204 RPE compared to anti-miR-con (Fig. 5d). Similar to miR-204$^{-/-}$ mice, TEM images of anti-miR-204 transfected RPE show increased accumulation of autophagic vacuoles compared to controls (Supplementary Material, Fig. S3e).

Notably, in the RPE of miR-204$^{-/-}$ mice and in human RPE transfected with anti-miR-204 there was an increase in expression of Rab22a (Fig. 5e–h), a direct target of miR-204 (29–31) implicated in preventing endosome maturation—required for fusion and transfer of cargo to lysosomes for proteolysis. WT mice exhibited relatively low levels of Rab22a expression at 8 a.m. (2 h after light onset coinciding with peak POS uptake (32)), and at 10 a.m. and 12 p.m., consistent with the RPE's maintenance of normally high levels of miR-204 expression (Fig. 5e, left). In contrast, the miR-204$^{-/-}$ mice exhibited relatively higher levels of Rab22a expression at the time points indicated (Fig. 5e, right). The increase in Rab22a in miR-204$^{-/-}$ RPE was corroborated by western blots ($n = 4$; Fig. 5f). In addition, higher levels of Rab22a immunostaining was observed in hfRPE cells transfected with anti-miR-204 following POS feeding for 4 h (mimicking the *in vivo* condition at 10 a.m., 4 h after light/phagocytosis onset; Fig. 5g). In the KO, the increased Rab22a levels suggest a dysregulation whose locus is the intersection of the autophagy and endosome pathways. These results suggest an imbalance in endocytic uptake, degradation and recycling that result in the persistent accumulation of rhodopsin.

In vivo, it is possible that microglia arrival at the RPE is stimulated by miR-204-induced changes in the RPE's cytokine or chemoattractant profiles. This hypothesis was tested *in vitro* using hfRPE. Apical and basal media were collected ($n = 3$ hfRPE donors) from anti-miR-control and anti-miR-204 transfected cells (4 or 9 days) and measured for known cytokine/chemokines for microglial cells, including CCL2, CCL7, CCL13, CCL22, CXCL10, IL-6, IL-11, CCL3, CCL8, CCL17, CxCl2, ICAM1, IL-8, CXCL13/Fractalkine, IL-1 beta, CCL5/RANTES, TNF-alpha, GM-CSF and CL12/SDF-1a. Only the apical levels of IL-8 were significantly increased (∼2-fold) in anti-miR-204 treated cells (9 days post-transfection; Fig. 5i, $P = 0.02$). Figures 4 and 5 indicate that the reduction or complete loss of miR-204 disrupts normal endocytic and autophagic pathways and causes the accumulation of rhodopsin and the polarized secretion of IL-8 (Figs 4a–c and 5c, d and i). The latter perhaps creating a chemokine gradient that *in vivo* could attract the resident retinal microglial cells to the RPE cell layer and provide a platform for the observed autofluorescence (Fig. 1).

Discussion

Previously, we showed that anti-miR-204 significantly disrupts the integrity of human RPE tight junction proteins and overall epithelial phenotype, including transport potential and barrier

function (9). miR-204 knockdown also significantly reduced the expression of RPE visual cycle genes, LRAT, RPE65 and TTR, needed for photoreceptor visual pigment regeneration (33). miR-204 is highly expressed in RPE (copy number ≈ 10 000), even compared to housekeeping genes, (34) supporting the notion that RPE miR-204 plays a critical role in maintaining homeostasis of the neural retina and SRS. This is further supported by preliminary studies on RPE-conditional miR-204 KO mice that exhibited autofluorescence accumulation and abnormal electrophysiological responses (C. Zhang, *et al.*, *Invest Ophtalmol Vis Sci.* 2017;58:ARVO E-Abstract 3568) similar to the global KO. Thus, despite some expression in retinal neuronal subtypes, RPE miR-204 (expression ≈40-fold greater than retina) (9) is very likely a major determinant of visual function in the retina/RPE complex.

The global KO mouse (*in vivo/mouse*) and human (*in vitro*) data were used to construct the schematic model shown in Figure 6. Permanent loss of miR-204 (months) ultimately leads to homeostatic imbalance contributing to retinal and RPE structural damage and loss of function. More specifically, reductions in miR-204 relieves inhibition on Rab22a, an inhibitor of endosomal maturation. Despite evidence of an increase in autophagy-related gene expression, both the miR-204$^{-/-}$ mice and human RPE cultures pre-treated with anti-miR-204 revealed an *accumulation* of undigested POS following photoreceptor phagocytosis, indicating a blockage of phagolysosomal activity.

This seemingly contradictory result has been obtained in other systems where overexpression of autophagic markers, in late-stage disease, accompanies a deficit in lysosomal function and the subsequent accumulation of undigested materials (17,35,36). Indeed, features reminiscent of elevated autophagy have been reported in AMD donor tissues and in a mouse model of premature aging (37–39).

Consistent with these reports, TGF-β-2 is overexpressed in the RPE of AMD donor eyes afflicted with choroidal neovascularization/macular degeneration and in the vitreous aspirates of patients with proliferative vitreoretinopathy (40,41). The physiological impact of increased TGF-β-2 levels in AMD patients may in part depend on the homeostatic balance of
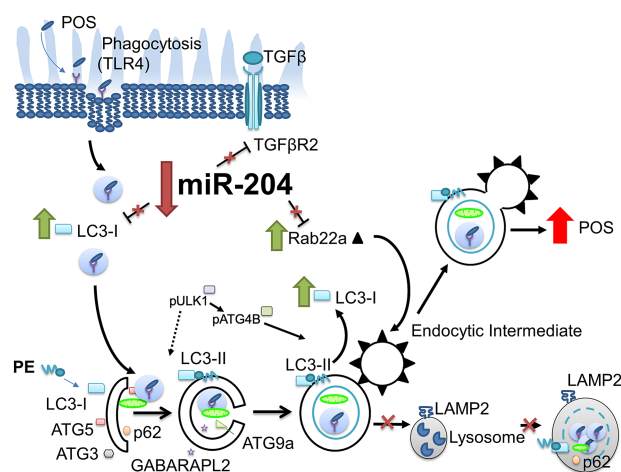

Figure 6. Model depicting knockdown or KO of miR-204 that disrupts autophagic expression and activity. Loss of miR-204 increases Rab22a expression that impedes maturation of early autophagosomal/endosomal intermediates that do not fuse with lysosomes (65) resulting in decreased phagocytic clearance. These changes in the autophagy-endolysosomal system lead to the accumulation of undigested POS inside the RPE.

miR-204 levels. *Reductions in miR-204 expression likely increase the availability of TGF-βR-2, which is one of its key direct targets located at the apical membrane of human RPE* (9,42). This increase can enhance the vulnerability of the RPE to TGF-β-induced trans-differentiation (43). Additionally, the diurnal phagocytic process of the RPE bears resemblance to the clearance of dead cells by the immune system in that they are normally immunologically silent (44). In AMD, one possibility is that accumulation of undigested POS leads to loss of immune silence and that pro-inflammatory responses are promoted by the arrival of Iba1+ microglial cells at the RPE (Supplementary Material, Fig. S2) and increased RPE secretion of IL-8 (45). We speculate that the normally high levels of RPE miR-204 are fundamentally important for avoiding TGF-β-induced inflammatory responses, thus protecting the RPE and surrounding cells and preserving vision.

POSs are rich in polyunsaturated fatty acids vulnerable to photo-oxidation (46). Inefficient clearance of POS results in oxidative stress stimulating the RPE to secrete soluble cytokines that initiate recruitment of phagocytic Iba1+ microglia to the SRS. Lei *et al.* (21) have shown that microglia preferentially phagocytose and incompletely digest oxidized outer segments rapidly accumulating lipofuscin-like autofluorescence. These AF signals were notably increased at 6 months in the miR-204−/− mice and are also consistent with increased numbers of morphologically altered Iba1+ microglial cells that migrated to the RPE at 9 months of age. The age-related increase in lipofuscin-like deposits in miR-204−/− mice are correlated with histologic findings and consistent with disease progression and aging in the human eye (47).

The autofluorescence in miR-204−/− mice (Fig. 1b) is also an indication of abnormal RPE metabolic activity associated with impaired photoreceptor phagocytosis and retinoid recycling (21). This impairment at 10 months perhaps results from a significant loss in RPE mitochondria, a reduced number of photoreceptors and disorganization of the IPM (Fig. 2b). The observed IPM dis-organization, induced by loss of miR-204, could impede the diffusion of *all-trans* retinol by interphotoreceptor binding proteins and reduce the rate of *11-cis*-retinal recycling. A small but significant loss of TTR activity (9) may also contribute to this effect and the observed reduction in a-wave response amplitude (Fig. 3a). The reduced b-wave amplitudes recorded in mice lacking miR-204 imply reduced synaptic transmission (Fig. 3b).

The accumulation of lipofuscin-like autofluorescence and disruption of the IPM and its protein constituents (48) are also observed in human inherited retinal diseases and provide a proximate cause for the significant reductions in the retinal ERG a- and b-wave responses observed in the mouse miR-204−/− (Fig. 3a and b; Supplementary Material, Tables S1 and S2).

The miR-204−/− mouse also exhibited significant reductions in the DC-ERG recorded c-wave and FO (Fig. 3g and h; Supplementary Material, Table S3). The c-wave is the sum of two components: (1) a positive potential across the RPE generated in response to a light-evoked decrease of $[K^+]_o$ in the SRS that hyperpolarizes the RPE apical membrane Kir 7.1 inwardly rectifying potassium (K) channels and (2) a slower, negative PIII component generated by inner retinal neurons (49). In contrast, the FO (50) is exclusively generated by the RPE as a delayed basolateral membrane hyperpolarization initiated following the light-induced decrease of SRS $[K]_o$ and the subsequent reversal of the apical membrane Na, K, 2Cl cotransporter and reduction of intracellular K and Cl. The latter decrease hyperpolarizes the basolateral membrane cystic fibrosis transmembrane conductance regulator and generates the FO (51). The decrease

of miR-204 in human RPE has been shown to decrease Kir7.1 expression and thus likely limits K efflux across the RPE apical membrane (9), perhaps accounting for the reduced amplitude of the mouse DC ERG c-wave. In addition, the Kir 7.1 K channels are functionally coupled to other apical membrane K transporters and the recycling capacity of this channel is maintained by normally high levels of miR-204 expression (52). In the mir-204−/− model or as miR-204 levels drop, K recycling decreases and intracellular K likely accumulates in the RPE and contributes to create cell swelling and the observed (possibly osmotic) disruption of SRS membrane structures that can contribute to autophagy induction.

The data in Figure 3 show a loss of retinal and RPE function (significant reduction of a- and b-wave amplitudes as well as RPE c-wave and FO amplitudes) in the miR-204 global KO. This loss could have been generated by a decrease in miR-204 in retina or RPE. The miR-204 expression levels are much higher (42-fold) in RPE compared to retina (9). To further address this question, we have initiated studies on RPE-conditional miR-204−/− mice (C. Zhang, *et al.*, submitted for publication). These mice show a similar retinal electrophysiological phenotype (data not shown) to the global KO, thus the reduction in a-wave and b-wave amplitudes is most likely attributed to the loss of miR-204 expression in the RPE *per se*.

In addition, we have considered the nature of the light source (7 min stimuli, 10 scotopic cd m−2) used to generate the relatively slow components of the RPE response to photoreceptor activity. We estimate that 11% of the visual pigment was bleached under these experimental conditions (53). Such a bleach would be anticipated to reduce rod sensitivity by 50% (∼2-fold), (54) resulting from persistent bleached pigment. In the rod-dominated mouse eye, the RPE is the principal site through which the light-absorbing chromophore, 11-*cis* retinal is regenerated. In miR-204−/− mice, the inefficient delivery of 11-*cis* retinal back to the photoreceptors likely arises from the reduced expression of RPE visual cycle genes (LRAT, RPE65 and TTR) (55), and the incomplete degradation of POS and lysosomal accumulation of rhodopsin, limiting the supply of chromophore for regeneration of bleached pigment. *Given these observations, we conclude that the origin of the phenotypic changes observed in the miR-204−/−, including the DC-ERG, is initiated in large part by the loss of miR-204 in the RPE itself*.

Taken together, the present data show that miR-204 reduction is an important endogenous modifier of RPE pathophysiology. The retinal degeneration observed in the miR-204 KO mouse (Figs. 1–3) is reminiscent of ocular and other human diseases in which decreased miR-204 or altered endolysosomal function plays a significant role in disease progression (56). The reduction in miR-204 levels concomitant with an alteration in autophagy and endolysosomal interactions (Fig. 6) are sentinels of metabolic dysregulation. Collectively, the present results provide a direct association between the global loss of miR-204 and increased expression of Rab22a leading to RPE/retinal degeneration suggesting both miR-204 and Rab22a as novel targets for therapeutic intervention (3,9,11,12).

Materials and Methods

Mice

Mice were maintained and tested according to standard conditions outlined in the animal study protocol approved by Animal Care and Use Committee of the National Eye Institute. All mice were genotyped and screened to be negative for the spontaneous

rd8 frameshift mutation, which causes retinal degeneration and is naturally occurring in C57BL/6N strains (57). See Supplementary Materials and Methods for generation and validation of mir-$204^{-/-}$ mice.

In vivo imaging. Ocular structure was evaluated *in vivo* by fundus examination and OCT. For all *in vivo* imaging techniques, animals were placed under anesthesia via a subcutaneous injection of a ketamine/xylazine mixture (i.p. 100 mg/kg and 6 mg/kg, respectively). Pupils were dilated with phenylephrine (2.5%) and tropicamide (1%). A drop of GenTeal Gel (Novartis) was placed on each eye to prevent desiccation.

Fundus photographs of mice (age 6 weeks and 6 months) were taken with a Micron-2 camera (Phoenix Research Laboratories, Inc., Pleasanton, CA) using StreamPix 5 software. Retinal OCT images were obtained using either a Heidelberg Spectralis HRA+OCT system (Heidelberg Engineering, Franklin, MA) or the Envisu UHR2200 (Bioptigen, Durham, NC). For OCT images obtained on the Spectralis HRA+OCT system, eye motion artifacts were eliminated by in-system eye tracking. Each B-scan image was averaged from 10 to 25 frames to increase the signal-to-noise ratio. A 30-degree lens was used for the OCT scan, and images were taken at high resolution HR, 1536×496, or at high speed (HS), 768×496. A 55-degree lens was used for the autofluorescence images (AF), and images were taken at HR, 1536×1536, or at HS, 768×768. In comparison to the Spectralis, the Envisu system employs a wider bandwidth (160 nm) for OCT beam and provides a higher axial resolution (1.6 μm in tissue).

Histopathology

Eyes were enucleated and fixed with 10% formalin for at least 24 h at room temperature (RT). Tissues were embedded in methacrylate and serially sectioned in the vertical pupillary optic nerve plane. Each eye was cut into six sections and stained with hematoxylin and eosin. If an ocular lesion was observed, then another 6–12 sections were cut through the lesion. Slides were also stained with periodic acid–Schiff to highlight Bruch's membrane and the basement membrane of small neovascular vessels.

Electron microscopy

Mouse eyes or cultured human fetal RPE were fixed in 2.5% glutaraldehyde + 2.5% paraformaldehyde in 0.1 M sodium cacodylate buffered solution (Electron Microscopy Sciences EMS, Hatfield, PA) at RT for 2 h and rinsed three times for 5 min in PBS. Tissues were then treated with 1% ice-cold osmium tetroxide in PBS solution for 1 h. After osmication, tissues were rinsed in PBS and processed through a battery of ethanol dehydration steps (three washes in 50, 70, 85 and 100% ethanol, respectively) for plastic embedding. A routine TEM protocol was used to obtain the RPE micrographs.

Immunostaining of mouse RPE or retina flat-mounts and hfRPE grown on transwells

Aged-matched mouse RPE or retina flat-mount tissues were dissected at 8 a.m., 10 a.m. and 12 p.m. coinciding with the peak of phagocytosis or activation of autophagy following phagocytosis in C57BL/6 transgenic mice as described in Yao *et al.* (58).

Mouse RPE or retina flat-mount tissues were prepared, washed in HBSS (−/−) and HEPES (10 mM) on ice and fixed in 4% paraformaldehyde/1× PBS (20 min) at RT. The tissues were permeabilized with immunocytochemistry (ICC) blocking buffer (1× PBST, 0.5% normal goat serum, 0.3% Triton X-100) for 1 h. RPE cell cultures grown on transwells were similarly fixed in 4% PFA added to the apical and basal compartments. For cultured RPE monolayers, exposure to the fixative was limited to 5–10 min at RT to prevent crosslinking of antigens and the masking of epitopes. Samples were washed 3× in PBST (1× PBS, 0.5% Tween20) and permeabilized and blocked for 1 h in an ICC blocking buffer containing (1× PBS, 1% BSA, 0.25% Tween20, 0.25% Triton X-100).

RPE was blocked and stained overnight at 4°C with primary antibodies recognizing either Rhodopsin (Abcam, Cat#: ab3424 or Encor, Cat#: MCA-A531), Iba1 (Wako Chemicals USA, Cat#: 019-19741), a specific marker for macrophages/microglia, LC3B (Cell Signaling Inc., Cat#: 2775S), Lamp1 (Abcam, 1:100, Cat#: ab24170), Lamp2 (Abcam, 1:100, Cat#: ab13524), Rab22a (Abcam, 1:250, Cat#: ab137093). After allowing time to equilibrate to RT, tissues were washed 3× in ICC buffer.

Where noted, RPE cell boundaries and nuclei were visualized with ZO-1 or Alexa Fluor 488-phalloidin and DAPI/Hoechst 33342. Appropriate fluorescent secondary antibodies were added and incubated for 1 h at RT. Samples were subsequently washed 3× in ICC buffer and mounted onto glass slides using Fluoromount-G aqueous mounting medium (Southern Biotech, Cat#: 0100-01). Images were taken imaged on a Zeiss Axio Imager M2 inverted fluorescent microscope with Apotome 2 and Zen 2012 software (Carl Zeiss AG) or a Zeiss 800 confocal microscope. All similarly stained samples were imaged under the same exposure times and adjusted to the same contrast settings before being exported.

Image quantification of LAMP2 signals in cultured human fetal RPE

Images of RPE transfected with anti-miR-con ($n = 5$) or anti-miR-204 ($n = 5$) were selected for analysis. For image quantification, the green channel (corresponding to LAMP2) of the MIP RGB image (magnification, 63×) was isolated and the mean image intensity measured in ImageJ. The average cell signal intensities were normalized against the number of cells within the field of view. To count the number of cells (approximated by the number of nuclei), the blue channel (corresponding to Hoechst 33342) was converted to an 8-bit grayscale image in ImageJ. An image threshold was manually adjusted to highlight the individual nuclei and to create a black and white binary image. Particle counting included all circularity and limited sizes (in pixels) between 200-infiniti. The measured integrated density (area∗mean gray value) of LAMP2 signals was then normalized to the number of cells to obtain the fluorescence intensity per cell (a.u.).

Electrophysiological recordings

Age-matched animals were dark adapted overnight (>12 h) and prepared for electrophysiological recordings under dim red light. Pupils were dilated with 2.5% phenylephrine HCl and 0.5% tropicamide. Corneal anesthesia was provided with 0.5% proparacaine HCl, and 2.5% hypromellose demulcent solution kept the eye hydrated throughout the recording. An Espion E2 ERG recording system with ColorDome Ganzfeld illumination (Diagnosys LLC, Lowell, MA), fitted with a heated mouse table (37°C), was used to obtain dark-adapted ERG recordings.

Visual stimuli consisted of flashes of light at varying intensities (0.0001, 0.001, 0.01, 0.1, 1, 10 cd s/m^2) with sufficient intervals between each stimulus presented. DC-ERGs were recorded using glass capillary tubes filled with Hank's buffered salt solution (HBSS). Electrodes remained in contact with the cornea at least 10 minutes prior to the recording to facilitate steady-state conditions.

Electrophysiological data analysis

Photoresponses were stored on a computer for offline analysis performed in MATLAB. Prior to processing, the ERG responses were digitally filtered with a low-frequency cutoff of 25 Hz. Amplitudes of the a-wave and b-wave were determined by defining a time window following light onset to determine the maxima between 25–70 ms or 65–175 ms, respectively. The b-wave was defined in reference to the amplitude of the a-wave ($b_{wave} = b_{max} - a_{max}$).

Prior to processing, the DC-ERG traces were smoothed with a moving average filter that spans 5 points (~5 ms) and drift-corrected by subtracting the best fit line through the time points preceding light onset. The components of the DC-ERG were then independently measured to determine the amplitudes of the c-wave, FO and OFF. The LP, defined as the gradual increase in the standing potential in response to maintained illumination, is measured from the trough of the FO until it plateaus just prior to the beginning of the OFF.

miR-204 knockdown in human fetal RPE

Primary cultures of human fetal RPE (59,60) were seeded onto transwell cell culture inserts (Corning Costar, Corning, NY) and allowed to mature for at least 8 weeks under normal (5% CO_2, 20% O_2) cell culture conditions. Selected transwells were transfected for 4 or 9 days with anti-miRNA oligonucleotides using 200 nM miRIDIAN microRNA human hsa-miR-204-5p inhibitor or miRIDIAN microRNA Inhibitor Negative Control 2 and dharmafect 4 as transfection reagent (Dharmacon, Lafayette, CO).

Gene and miR expression by qRT-PCR

Total RNA was obtained from cell culture lysate (hfRPE grown on transwells) or RPE/choroid tissues dissected from eyes of WT or mir-204$^{-/-}$ mice. Tissues were collected in 600 µl of lysis/binding buffer (mirVana miRNA isolation kit) and frozen until extraction of total RNA, according to manufacturer's manual. All hfRPE samples were grown in culture for at least 8 weeks prior to collection. All mice used for gene/miR expression analysis were between 6 and 9 months old, and RPE samples were collected at ~12 p.m.

For miR analysis of mouse and human RPE, all reagents were purchased from Applied Biosystems Inc. The RT reactions were performed using a miR reverse transcription kit according to the manufacturer's instructions. SnoRNA202 and snoRNA234 were chosen as internal controls for normalization for mouse tissue. Let-7a and hsa-miR-16 were used as normalization controls for human tissue.

For gene expression analysis of mouse RPE, reverse transcription of mRNA to cDNA was performed using a SuperScript III First-Strand Synthesis kit (catalog no. 11904-018; Thermo Fisher Scientific). The cDNA was diluted to 1 ng/µl. A custom-made 88 gene PrimePCR Custom 384 well plate was purchased and developed using validated primer sets (catalog no. 100-25214; Bio-Rad Laboratories, Inc.). qPCR was run using RT^2 SYBR Green qPCR Mastermix (catalog no. 330503; Qiagen) according to manufacturer's protocol on a ViiA 7 Real-Time PCR System (Thermo Fisher Scientific). Three housekeeping genes (HPRT, TBP and GAPDH) were used as internal controls. Genes with non-detectable Ct values in both miR-204$^{-/-}$ and littermate controls were removed from analysis. A volcano plot was used to visualize the gene expression data, highlighting differentially expressed genes with greater than 2-fold change in expression.

Relative quantification was calculated using the $2^{-\Delta\Delta CT}$ method (61). Statistical significance was determined using Student's t-test (two-tailed, paired) with a level of significance of $P < 0.05$. The data are represented as fold change relative to control (2^n) for >3 biological samples.

Western blot analysis of RPE isolated from mouse or primary cultures of hfRPE

hfRPE cells grown on transwells or RPE tissue isolated from selected mice were lysed in 200 µl RIPA buffer (Thermo Fisher Scientific) containing protease inhibitor (Thermo Fisher Scientific). RPE tissue was dissected from mouse eyes (8 a.m., 10 a.m. or 12 p.m.), and total protein were extracted following an established protocol (62). Protein lysates were separated by electrophoresis and transferred to a PVDF membrane. Equal protein loading was confirmed by BCA per manufacturer's instructions. Non-specific binding was blocked with 5% BSA in PBST. Membranes were incubated overnight at 4°C with primary antibodies (1:1000) against rhodopsin (Encor, Cat#: MCA-A531), LC3B (Cell Signaling Inc., Cat#: 2775S), p62/SQTM1 (D5E2) (Cell Signaling Inc., Cat#: 8025S), Rab22a (Abcam, Cat#: ab137093), ULKL1 (Abcam, Cat#: ab167139) and anti-β-Actin (protein loading control, Sigma, Cat#: A1978, 1:2000) or β-tubulin (protein loading control, EMD Millipore, Cat#: MAB1637, 1:2000). Membranes were subsequently washed 3× in PBST, followed by incubation with secondary antibodies (IR dye 800 and 680) for 45 min at RT. Western blots were imaged using the Odyssey Infrared Imaging System (LI-COR, Ody-3120) or Bio-Rad ChemiDoc MP Imaging System.

Phagocytosis uptake and digestion measured by flow cytometry, IF and WB

Phagocytosis experiments were performed on confluent polarized cultures of human fetal RPE. Phagocytosis uptake was assessed by feeding ~10 POS/RPE for 4 h with pHrodo-labeled bovine outer segments. Phagocytosis digestion was performed by feeding ~10 POS/RPE cell for 4 h with pHrodo-labeled bovine outer segments followed by a wash (removal of POS) and allowing the RPE to digest the phagocytosed POS for 24 h prior to FACS analysis. RPE were trypsinized with 0.25% trypsin for ~30 min and strained through a 40 µm filter to achieve single cell suspensions for FACS analysis. Cells were resuspended in FACS buffer (2% FBS in D-PBS) containing DAPI (40 ng/ml) for determining viability. A FACS analysis was performed using FlowJo software. Due to donor variability, the results of each experiment were normalized to the average value of the corresponding negative control (anti-miR-con) for each donor. The results were collected from two separate experiments using two different hfRPE donors ($n = 3$ each).

Phagocytic accumulation of rhodopsin in hfRPE was also determined by immunofluorescence and western blot (see appropriate sections) following 4 h feeding with 40 POS/RPE + MFG-E8 (2.5 µg/ml) + protein S (2 µg/ml). The glycoprotein, milk fat globule EGF-8 (MFG-E8) and protein S are

phagocytic ligands ('eat-me signal') secreted by the RPE that have been shown to stimulate POS phagocytosis (63,64).

Cytokine/chemokine secretion of hfRPE

hFRPE were grown on transwells and transfected with anti-miR-con or anti-miR-204 for 4 or 9 days. Apical and basal media were collected from $n = 3$ donors and assayed using the human Magnetic Luminex Assay (R&D Systems) for various cytokines/chemokines (including CCL2, CCL7, CCL13, CCL22, CXCL10, IL-6, IL-11, CCL3, CCL8, CCL17, CxCl2, ICAM1, CXCL8/IL-8, CXCL13/Fractakine, IL-1 beta, CCL5/RANTES, TNF-alpha, GM-CSF and CL12/SDF-1a) reported to be known chemoattractants for macrophage/microglial cells.

Statistical analysis

Paired (two-tailed) sample *t*-test analysis was used to determine statistically significant differences ($P < 0.05$) between WT and miR-204$^{-/-}$ mice or between anti-miR-con and anti-miR-204-transfected human fetal RPE. All data represented as mean $\pm$ standard error.

Funding

Acknowledgements

References

1. Felekkis, K., Touvana, E., Stefanou, C. and Deltas, C. (2010) microRNAs: a newly described class of encoded molecules that play a role in health and disease. *Hippokratia*, **14**, 236–240.
2. Conte, I., Hadfield, K.D., Barbato, S., Carrella, S., Pizzo, M., Bhat, R.S., Carissimo, A., Karali, M., Porter, L.F., Urquhart, J. *et al.* (2015) MiR-204 is responsible for inherited retinal dystrophy associated with ocular coloboma. *Proc. Natl. Acad. Sci. U. S. A.*, **112**, E3236–E3245.
3. Courboulin, A., Paulin, R., Giguère, N.J., Saksouk, N., Perreault, T., Meloche, J., Paquet, E.R., Biardel, S., Provencher, S., Côté, J., Simard, M.J. and Bonnet, S. (2011) Role for miR-204 in human pulmonary arterial hypertension. *J. Exp. Med.*, **208**, 535–548.
4. Butrym, A., Rybka, J., Baczyńska, D., Tukiendorf, A., Kuliczkowski, K. and Mazur, G. (2015) Low expression of microRNA-204 (miR-204) is associated with poor clinical outcome of acute myeloid leukemia (AML) patients. *J. Exp. Clin. Cancer Res.*, **34**, 68.
5. Lee, H., Lee, S., Bae, H., Kang, H.S. and Kim, S.J. (2016) Genome-wide identification of target genes for miR-204 and miR-211 identifies their proliferation stimulatory role in breast cancer cells. *Sci. Rep.*, **6**, 25287.
6. Hall, D.P., Cost, N.G., Hegde, S., Kellner, E., Mikhaylova, O., Stratton, Y., Ehmer, B., Abplanalp, W.A., Pandey, R., Biesiada, J. *et al.* (2014) TRPM3 and miR-204 establish a regulatory circuit that controls oncogenic autophagy in clear cell renal cell carcinoma. *Cancer Cell*, **26**, 738–753.
7. Wang, P., Lv, H.Y., Zhou, D.M. and Zhang, E.N. (2016) miR-204 suppresses non-small-cell lung carcinoma (NSCLC) invasion and migration by targeting JAK2. *Genet. Mol. Res.*, **15**, 1–9.
8. Mazar, J., Qi, F., Lee, B., Marchica, J., Govindarajan, S., Shelley, J., Li, J.L., Ray, A. and Perera, R.J. (2016) MicroRNA 211 functions as a metabolic switch in human melanoma cells. *Mol. Cell. Biol.*, **36**, 1090–1108.
9. Wang, F.E., Zhang, C., Maminishkis, A., Dong, L., Zhi, C., Li, R., Zhao, J., Majerciak, V., Gaur, A.B., Chen, S. *et al.* (2010) MicroRNA-204/211 alters epithelial physiology. *FASEB J.*, **24**, 1552–1571.
10. Yin, Y., Zhang, B., Wang, W., Fei, B., Quan, C., Zhang, J., Song, M., Bian, Z., Wang, Q., Ni, S. *et al.* (2014) miR-204-5p inhibits proliferation and invasion and enhances chemotherapeutic sensitivity of colorectal cancer cells by downregulating RAB22A. *Clin. Cancer Res.*, **20**, 6187–6199.
11. Guo, W., Zhang, Y., Shi, Y., Xi, J., Fan, H. and Xu, S. (2015) Decreased expression of miR-204 in plasma is associated with a poor prognosis in patients with non-small cell lung cancer. *Int. J. Mol. Med.*, **36**, 1720–1726.
12. Li, W., Jin, X., Zhang, Q., Zhang, G., Deng, X. and Ma, L. (2014) Decreased expression of miR-204 is associated with poor prognosis in patients with breast cancer. *Int. J. Clin. Exp. Pathol.*, **7**, 3287–3292.
13. Li, T., Pan, H. and Li, R. (2016) The dual regulatory role of miR-204 in cancer. *Tumour Biol.*, **37**, 11667–11677.
14. Liu, Z., Long, J., Du, R., Ge, C., Guo, K. and Xu, Y. (2016) miR-204 regulates the EMT by targeting snai1 to suppress the invasion and migration of gastric cancer. *Tumour Biol.*, **37**, 8327–8335.
15. Filios, S.R. and Shalev, A. (2015) β-cell microRNAs: small but powerful. *Diabetes*, **64**, 3631–3644.
16. Silverman, S.M. and Wong, W.T. (2018) Microglia in the retina: roles in development, maturity, and disease. *Annu. Rev. Vis. Sci*, **4**, 45–77.
17. Wang, A.L., Lukas, T.J., Yuan, M., Du, N., Tso, M.O. and Neufeld, A.H. (2009) Autophagy and exosomes in the aged retinal pigment epithelium: possible relevance to drusen formation and age-related macular degeneration. *PLoS One*, **4**, e4160.
18. Karali, M., Manfredi, A., Puppo, A., Marrocco, E., Gargiulo, A., Allocca, M., Corte, M.D., Rossi, S., Giunti, M., Bacci, M.L. *et al.* (2011) MicroRNA-restricted transgene expression in the retina. *PLoS One*, **6**, e22166.
19. Stockton, R.A. and Slaughter, M.M. (1989) B-wave of the electroretinogram. A reflection of ON bipolar cell activity. *J. Gen. Physiol.*, **93**, 101–122.
20. Steinberg, R.H., Linsenmeier, R.A. and Griff, E.R. (1983) Three light-evoked responses of the retinal pigment epithelium. *Vision Res.*, **23**, 1315–1323.
21. Lei, L., Tzekov, R., Tang, S. and Kaushal, S. (2012) Accumulation and autofluorescence of phagocytized rod outer segment material in macrophages and microglial cells. *Mol. Vis.*, **18**, 103–113.
22. Strunnikova, N.V., Maminishkis, A., Barb, J.J., Wang, F., Zhi, C., Sergeev, Y., Chen, W., Edwards, A.O., Stambolian, D., Abecasis, G. *et al.* (2010) Transcriptome analysis and molecular signature of human retinal pigment epithelium. *Hum. Mol. Genet.*, **19**, 2468–2486.

23. Miyagishima, K.J., Wan, Q., Corneo, B., Sharma, R., Lotfi, M.R., Boles, N.C., Hua, F., Maminishkis, A., Zhang, C., Blenkinsop, T. *et al.* (2016) Pursuit of authenticity: induced pluripotent stem cell-derived retinal pigment epithelium for clinical applications. *Stem Cells Transl. Med.*, **5**, 1562–1574.

24. Miyagishima, K.J., Wan, Q., Miller, S.S. and Bharti, K. (2017) A basis for comparison: sensitive authentication of stem cell derived RPE using physiological responses of intact RPE monolayers. *Stem Cell Transl. Investig.*, **4**, 1–5.

25. Pengo, N., Agrotis, A., Prak, K., Jones, J. and Ketteler, R. (2017) A reversible phospho-switch mediated by ULK1 regulates the activity of autophagy protease ATG4B. *Nat. Commun.*, **8**, 294.

26. Zachari, M. and Ganley, I.G. (2017) The mammalian ULK1 complex and autophagy initiation. *Essays Biochem.*, **61**, 585–596.

27. Bjørkøy, G., Lamark, T., Pankiv, S., Øvervatn, A., Brech, A. and Johansen, T. (2009) Monitoring autophagic degradation of p62/SQSTM1. *Methods Enzymol.*, **452**, 181–197.

28. Cook, K.L., Soto-Pantoja, D.R., Abu-Asab, M., Clarke, P.A., Roberts, D.D. and Clarke, R. (2014) Mitochondria directly donate their membrane to form autophagosomes during a novel mechanism of parkin-associated mitophagy. *Cell Biosci.*, **4**, 16.

29. Xia, Z., Liu, F., Zhang, J. and Liu, L. (2015) Decreased expression of miRNA-204-5p contributes to glioma progression and promotes glioma cell growth, migration and invasion. *PLoS One*, **10**, e0132399.

30. Mesa, R., Salomón, C., Roggero, M., Stahl, P.D. and Mayorga, L.S. (2001) Rab22a affects the morphology and function of the endocytic pathway. *J. Cell Sci.*, **114**, 4041–4049.

31. Roberts, E.A., Chua, J., Kyei, G.B. and Deretic, V. (2006) Higher order Rab programming in phagolysosome biogenesis. *J. Cell Biol.*, **174**, 923–929.

32. Yu, B., Egbejimi, A., Dharmat, R., Xu, P., Zhao, Z., Long, B., Miao, H., Chen, R., Wensel, T.G., Cai, J. and Chen, Y. (2018) Phagocytosed photoreceptor outer segments activate mTORC1 in the retinal pigment epithelium. *Sci. Signal.*, **11**, 1–11.

33. Kiser, P.D., Golczak, M. and Palczewski, K. (2014) Chemistry of the retinoid (visual) cycle. *Chem. Rev.*, **114**, 194–232.

34. Barber, R.D., Harmer, D.W., Coleman, R.A. and Clark, B.J. (2005) GAPDH as a housekeeping gene: analysis of GAPDH mRNA expression in a panel of 72 human tissues. *Physiol. Genomics*, **21**, 389–395.

35. Ost, A., Svensson, K., Ruishalme, I., Brännmark, C., Franck, N., Krook, H., Sandström, P., Kjolhede, P. and Strålfors, P. (2010) Attenuated mTOR signaling and enhanced autophagy in adipocytes from obese patients with type 2 diabetes. *Mol. Med.*, **16**, 235–246.

36. Whyte, L.S., Lau, A.A., Hemsley, K.M., Hopwood, J.J. and Sargeant, T.J. (2017) Endo-lysosomal and autophagic dysfunction: a driving factor in Alzheimer's disease? *J. Neurochem.*, **140**, 703–717.

37. Carroll, B., Hewitt, G. and Korolchuk, V.I. (2013) Autophagy and ageing: implications for age-related neurodegenerative diseases. *Essays Biochem.*, **55**, 119–131.

38. Mitter, S.K., Rao, H.V., Qi, X., Cai, J., Sugrue, A., Dunn, W.A., Grant, M.B. and Boulton, M.E. (2012) Autophagy in the retina: a potential role in age-related macular degeneration. *Adv. Exp. Med. Biol.*, **723**, 83–90.

39. Zhang, Y., Cross, S.D., Stanton, J.B., Marmorstein, A.D., Le, Y.Z. and Marmorstein, L.Y. (2017) Early AMD-like defects in the RPE and retinal degeneration in aged mice with RPE-specific deletion of Atg5 or Atg7. *Mol. Vis.*, **23**, 228–241.

40. Kliffen, M., Sharma, H.S., Mooy, C.M., Kerkvliet, S. and de Jong, P.T. (1997) Increased expression of angiogenic growth factors in age-related maculopathy. *Br. J. Ophthalmol.*, **81**, 154–162.

41. Connor, T.B., Jr., Roberts, A.B., Sporn, M.B., Danielpour, D., Dart, L.L., Michels, R.G., de Bustros, S., Enger, C., Kato, H., Lansing, M. *et al.* (1989) Correlation of fibrosis and transforming growth factor-beta type 2 levels in the eye. *J. Clin. Invest.*, **83**, 1661–1666.

42. Szemraj, M., Bielecka-Kowalska, A., Oszajca, K., Krajewska, M., Goś, R., Jurowski, P., Kowalski, M. and Szemraj, J. (2015) Serum microRNAs as potential biomarkers of AMD. *Med. Sci. Monit.*, **21**, 2734–2742.

43. Dvashi, Z., Goldberg, M., Adir, O., Shapira, M. and Pollack, A. (2015) TGF-β1 induced transdifferentiation of rpe cells is mediated by TAK1. *PLoS One*, **10**, e0122229.

44. Green, D.R., Oguin, T.H. and Martinez, J. (2016) The clearance of dying cells: table for two. *Cell Death Differ.*, **23**, 915–926.

45. Ma, W., Zhao, L., Fontainhas, A.M., Fariss, R.N. and Wong, W.T. (2009) Microglia in the mouse retina alter the structure and function of retinal pigmented epithelial cells: a potential cellular interaction relevant to AMD. *PLoS One*, **4**, e7945.

46. Qin, S. and Rodrigues, G.A. (2008) Progress and perspectives on the role of RPE cell inflammatory responses in the development of age-related macular degeneration. *J. Inflamm. Res.*, **1**, 49–65.

47. Bonilha, V.L. (2008) Age and disease-related structural changes in the retinal pigment epithelium. *Clin. Ophthalmol.*, **2**, 413–424.

48. Ishikawa, M., Sawada, Y. and Yoshitomi, T. (2015) Structure and function of the interphotoreceptor matrix surrounding retinal photoreceptor cells. *Exp. Eye Res.*, **133**, 3–18.

49. Witkovsky, P., Dudek, F.E. and Ripps, H. (1975) Slow PIII component of the carp electroretinogram. *J. Gen. Physiol.*, **65**, 119–134.

50. Wu, J., Peachey, N.S. and Marmorstein, A.D. (2004) Light-evoked responses of the mouse retinal pigment epithelium. *J. Neurophysiol.*, **91**, 1134–1142.

51. Blaug, S., Quinn, R., Quong, J., Jalickee, S. and Miller, S.S. (2003) Retinal pigment epithelial function: a role for CFTR? *Doc. Ophthalmol.*, **106**, 43–50.

52. Rymer, J., Miller, S.S. and Edelman, J.L. (2001) Epinephrine-induced increases in [Ca2+](in) and KCl-coupled fluid absorption in bovine RPE. *Invest. Ophthalmol. Vis. Sci.*, **42**, 1921–1929.

53. Lyubarsky, A.L., Daniele, L.L. and Pugh, E.N. (2004) From candelas to photoisomerizations in the mouse eye by rhodopsin bleaching in situ and the light-rearing dependence of the major components of the mouse ERG. *Vision Res.*, **44**, 3235–3251.

54. Pahlberg, J., Frederiksen, R., Pollock, G.E., Miyagishima, K.J., Sampath, A.P. and Cornwall, M.C. (2017) Voltage-sensitive conductances increase the sensitivity of rod photoresponses following pigment bleaching. *J. Physiol.*, **595**, 3459–3469.

55. Kim, J.Y., Zhao, H., Martinez, J., Doggett, T.A., Kolesnikov, A.V., Tang, P.H., Ablonczy, Z., Chan, C.C., Zhou, Z., Green, D.R. *et al.* (2013) Noncanonical autophagy promotes the visual cycle. *Cell*, **154**, 365–376.

56. Mitter, S.K., Song, C., Qi, X., Mao, H., Rao, H., Akin, D., Lewin, A., Grant, M., Dunn, W., Ding, J., Rickman, C.B. amd Boulton, M. (2014) Dysregulated autophagy in the RPE is associated with increased susceptibility to oxidative stress and AMD. *Autophagy*, **10**, 1989–2005.

57. Mattapallil, M.J., Wawrousek, E.F., Chan, C.C., Zhao, H., Roy-choudhury, J., Ferguson, T.A. and Caspi, R.R. (2012) The Rd8 mutation of the Crb1 gene is present in vendor lines of C57BL/6N mice and embryonic stem cells, and confounds ocular induced mutant phenotypes. *Invest. Ophthalmol. Vis. Sci.*, **53**, 2921–2927.

58. Yao, J., Jia, L., Shelby, S.J., Ganios, A.M., Feathers, K., Thompson, D.A. and Zacks, D.N. (2014) Circadian and non-circadian modulation of autophagy in photoreceptors and retinal pigment epithelium. *Invest. Ophthalmol. Vis. Sci.*, **55**, 3237–3246.

59. Maminishkis, A., Chen, S., Jalickee, S., Banzon, T., Shi, G., Wang, F.E., Ehalt, T., Hammer, J.A. and Miller, S.S. (2006) Confluent monolayers of cultured human fetal retinal pigment epithelium exhibit morphology and physiology of native tissue. *Invest. Ophthalmol. Vis. Sci.*, **47**, 3612–3624.

60. Maminishkis, A. and Miller, S.S. (2010) Experimental models for study of retinal pigment epithelial physiology and patho-physiology. *J. Vis. Exp.*, **2010**, 2032.

61. Schmittgen, T.D. and Livak, K.J. (2008) Analyzing real-time PCR data by the comparative C(T) method. *Nat. Protoc.*, **3**, 1101–1108.

62. Wei, H., Xun, Z., Granado, H., Wu, A. and Handa, J.T. (2016) An easy, rapid method to isolate RPE cell protein from the mouse eye. *Exp. Eye Res.*, **145**, 450–455.

63. Nandrot, E.F., Anand, M., Almeida, D., Atabai, K., Sheppard, D. and Finnemann, S.C. (2007) Essential role for MFG-E8 as lig-and for alphavbeta5 integrin in diurnal retinal phagocytosis. *Proc. Natl. Acad. Sci. U. S. A.*, **104**, 12005–12010.

64. Müller, C., Charniga, C., Temple, S. and Finnemann, S.C. (2018) Quantified F-actin morphology is predictive of phago-cytic capacity of stem cell-derived retinal pigment epithe-lium. *Stem Cell Reports*, **10**, 1075–1087.

65. Ward, D.M., Pevsner, J., Scullion, M.A., Vaughn, M. and Kaplan, J. (2000) Syntaxin 7 and VAMP-7 are soluble N-ethylmaleimide-sensitive factor attachment protein recep-tors required for late endosome-lysosome and homotypic lysosome fusion in alveolar macrophages. *Mol. Biol. Cell*, **11**, 2327–2333.